Dielectronic satellite spectrum of heliumlike argon: A contribution to the physics of highly charged ions and plasma impurity transport

TFR Group[*]

Association EURATOM—CEA sur la Fusion, Commissariat a l'Energie Atomique, Département de Recherches sur la Fusion Contrôlée, Centre d'Etudes Nucléaires, Boîte Postale No. 6, 92260 Fontenay-aux-Roses, France

F. Bombarda

Associazione EURATOM—ENEA sulla Fusione, Centro Richerche Energia Frascati, Comitato Nazionale per la Ricerca e per lo Sviluppo dell'Energia Nucleare e delle Energie Alternative, Casella Postale 65, I-00044 Frascati, Rome, Italy

F. Bely-Dubau and P. Faucher

Observatoire de Nice, Boîte Postale No. 252, 06007 Nice Cedex, France

M. Cornille, J. Dubau, and M. Loulergue

Observatoire de Paris, 92190 Meudon, France

(Received 8 April 1985)

Wavelengths and atomic parameters for the satellite spectrum of the $1s^2$-$1s\,2p$ parent lines of Ar^{16+} have been calculated using a multiconfiguration intermediate-coupling scheme with a statistical Thomas-Fermi potential. These data, together with radial charge-state distributions given by an impurity transport code, are used to calculate theoretical spectra. The comparison with experimental x-ray spectra from the TFR tokamak plasma shows good agreement between calculated and observed wavelengths. The fitting of relative line intensities in the synthetic spectra to observed values improves the understanding of plasma impurity transport.

I. INTRODUCTION

The dielectronic satellite spectra from the heliumlike charge state of elements with medium atomic number (Mg to Fe) have important applications in the diagnosis of laboratory fusion plasmas as well as of solar flares.[1-3] Recently, tokamak plasma discharges have produced high-resolution spectra from Fe^{25+},[4] Cr^{22+},[5] Ti^{20+},[6] and Ar^{16+} (Refs. 7 and 8) showing the characteristic emission lines ($1s^2$-$1s\,2p$, $1s^2$-$1s\,2s$) of the heliumlike ions, and the satellite lines corresponding to the inner-shell radiative transitions $1s^2nl$-$1s\,2l'\,nl''$ ($n \geq 2$).

The high-quality spectra have stimulated atomic-physics calculations for several reasons. The steady-state phase of present-day tokamak plasmas is well characterized (typical electron temperatures are in the range from 1 to 3 keV) and tolerates seeding with various impurity elements, thus allowing the atomic-physics methods to be checked over a long isoelectronic series.[5,6] Computer codes used to interpret solar flare spectra[1,2] may be checked on laboratory plasmas. Finally, a deeper understanding of the complex production of these spectra (simply called satellite spectra in the following) may lead to a better description of phenomena which are not yet well understood or which will appear in conjunction with new methods of plasma heating or current generation, such as fast-relaxation and particle-transport phenomena, or excitation by electrons with non-Maxwellian velocity distribution or relativistic energies.

In this paper we present two x-ray spectra of argon ob- served under different plasma conditions and compare them with theoretical spectra obtained from extended *ab initio* atomic-physics calculations. The high signal-to-noise ratio of the observed spectra opens interesting insights into both the atomic theory of multiply charged ions and plasma diagnosis, in particular radial impurity transport.[9]

In Sec. II we give the experimental conditions. In Sec. III the TFR code for the impurity transport is summarized briefly and applied to observations in vacuum ultraviolet (vuv) spectroscopy. X-ray spectra obtained from crystal spectroscopy are presented in Sec. IV. The different atomic processes responsible for the argon satellite spectrum and the corresponding atomic parameters are given in Sec. V. These data together with calculated radial charge-state distributions (Sec. III) are then used to calculate synthetic spectra which are compared to observed ones (Sec. VI). In Sec. VII we briefly describe the determination of ion Doppler temperatures from line broadening.

II. EXPERIMENTAL CONDITIONS

For these argon injection experiments, the discharge conditions were: plasma current $I_p = 110$ kA, toroidal magnetic field $B_T = 28$ kG, limiter radius $a = 20$ cm, working gas H_2. The plasma current had a particularly long plateau, lasting from about 50 ms after breakdown to 400 ms (Fig. 1). The radial electron-temperature profile $T_e(r)$, as measured by Thomson scattering, remains con-
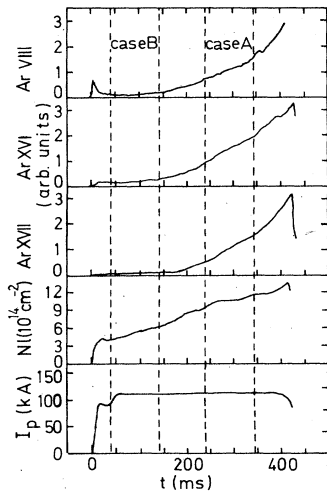
FIG. 1. Temporal behavior of argon line intensities, chord-integrated electron density and plasma current. The x-ray spectra were integrated over the intervals labeled A and B.

stant during the plateau phase with the central value $T_e(0) = 1.25$ keV, Fig. 2. However, the line-averaged electron density (Fig. 1) increases continuously. The electron-density profile (measured by HCN laser interferometry) has central values $n_e(0)$ of 2.1 and 5.8×10^{13} cm^{-3} at $t = 90$ and 290 ms, respectively [see Fig. 2 for $n_e(r)$ at $t = 290$ ms].

Argon is injected with the working gas, before breakdown and during the discharge. The recycling behavior of argon is not well understood. In particular we have observed that most of the argon is retained by the wall and/or limiters during the early phase of the discharge.
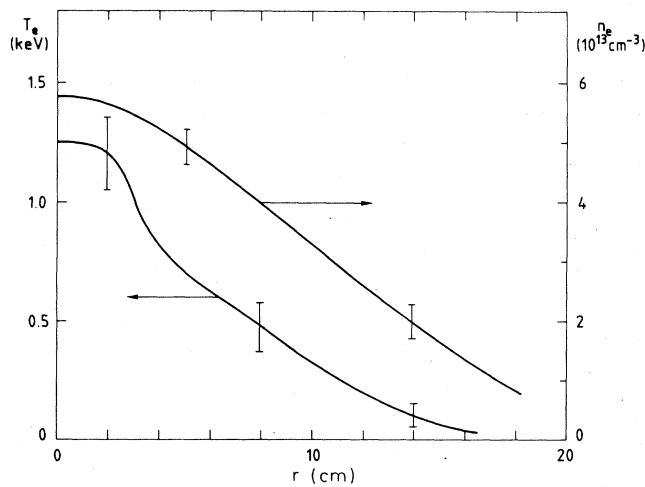

FIG. 2. Radial profiles of the electron temperature during the current plateau and of the electron density at $t = 290$ ms. For T_e, the solid line represents the mean of twenty 13-channel Thomson scattering profiles; the error bars indicate typical one-shot errors.

This is clearly demonstrated in Fig. 1, where we show the temporal behavior of the Ar VIII (700 Å), Ar XVI (354 Å), and Ar XVII (3.9 Å) lines. The initial peak on the Ar VIII signal gives evidence of the presence of argon at breakdown. However, the intensities of all spectral lines remain quite low up to an almost exponential increase which starts at $t \sim 150$ ms. More than half of the argon has been delivered by the valves at this time. This effect of early retention and progressive release of argon by the wall and limiter materials has two consequences. The first is that we cannot estimate the amount of argon in the plasma from the (measured) injection rate. The second is that only in the second half of the discharge we can make full use of our vuv spectroscopic equipment.[10] In particular this means that Abel inversion of the Ar XV and Ar XVI signals is possible in the interval from 240 to 340 ms (case A of x-ray crystal spectroscopy, Sec. IV), but hazardous between 40 and 140 ms (case B).

III. IMPURITY TRANSPORT CODE

Argon transport is studied by solving the impurity transport system in cylindrical geometry as a function of time (i.e., with toroidal and poloidal symmetry)

$$\frac{\partial n_Z}{\partial t} = -\frac{1}{r}\frac{\partial}{\partial r}(r\Gamma_Z) + n_e(n_{Z-1}S_{Z-1} - n_Z S_Z$$
$$+ n_{Z+1}\alpha_{Z+1} - n_Z\alpha_Z),$$
$$Z = 1, \ldots, 18 \quad (1)$$

where Γ_Z is the radial flux density (positive when directed outwards) of the argon ions of charge Z and n_Z are the corresponding ion densities; S_Z and α_Z are the rate coefficients for ionization and recombination, respectively. Since it is not possible to simulate the experimental data correctly using theoretical expressions for Γ_Z, adjustable ("anomalous") terms are added to Γ_Z. As these anomalous terms dominate, we use the simplified expression[10,11]

$$\Gamma_Z = -D_A\frac{\partial n_Z}{\partial r} - \frac{r}{a}V_A n_Z \quad (2)$$

with the adjustable parameters D_A (diffusion coefficient) and V_A (inward convection velocity). Both parameters are taken as independent of Z and r (spectroscopic observations have not yet clearly shown such a dependence). The dimensionless quantity $S = aV_A/2D_A$ is called the convection parameter.

The atomic-physics data (α_Z, S_Z) of the code have been described in Ref. 11. We have now added Auger ionization (inner-shell excitation above the ionization limit, followed by autoionization) according to Ref. 12. The code also includes a model for the population of excited levels and calculates the corresponding line emissivities $\epsilon(r)$ (photons cm^{-3} s^{-1}). In particular, for the strong $\Delta n = 0$ transitions (the vuv lines already mentioned), it is sufficient to use the coronal hypothesis: excitation is from the ground state, and deexcitation is only radiative. The excitation rate coefficients are obtained using the well-known g approximation.

The argon-ion distributions $n_Z(r)$ are obtained by solv-

ing the system (1) using expression (2) for Γ_Z with fixed values for D_A and V_A. Input data are the observed $n_e(r)$ and $T_e(r)$ profiles, and an initial argon-ion distribution (local ionization equilibrium with $\sum_Z n_Z$ independent of radius). The code is permitted to evolve to the steady-state solution, the number of particles being conserved by the last mesh boundary condition of complete recycling (i.e., the total outgoing ion flux is compensated by an equal incoming flux of argon atoms). Since the argon ions are pushed toward the center by the convection velocity V_A, the total argon-ion density $\sum_Z n_Z(r)$ will be peaked at $r=0$. The value of S determines the degree of peaking, and therefore the ratio of the radiance [line-of-sight integrated emissivity $\epsilon(r)$] of a highly ionized ion line (Ar XV or Ar XVI) to the radiance of a peripheral ion line (Ar VII or Ar VIII). The input values of D_A and V_A are varied until good agreement between code and experiment is obtained for one of the mentioned radiance ratios and for the emissivity profile $\epsilon(r)$ of a highly ionized ion line.

As already mentioned, we shall discuss two x-ray spectra of argon taken at high and low electron densities. We therefore apply the impurity transport code to these cases. Case A corresponds to the time interval from $t=240$ to 340 ms. As seen in Fig. 1, the electron density, and consequently the argon-line radiances, increases during this interval. However, the smooth behavior of all signals leads us to the hypothesis that the properties of the plasma at half-time of this interval, i.e., at $t=290$ ms, may be taken as representative for the whole interval. Therefore, we use for the code the electron-density profile taken at $t=290$ ms as shown in Fig. 2 (remember that the electron-temperature profile is quite constant over the duration of

the current plateau).

With $D_A=4000$ cm^{2}s^{-1} and $V_A=400$ cm s^{-1}, good agreement between code and experiment is obtained for the radial location of the emissivities of the two vuv argon lines, Ar XVI (354 Å) and Ar XV (221 Å). In particular, the code reproduces the shell-like emissivity profiles (Fig. 3), and the experimental and code values for the radii of maximum emission agree to within ± 1 cm (in the case of hollow emissivity profiles, the Abel inversion indicates the radial position of the maximum with good accuracy but is less reliable for the wings).

It is interesting to note here, that the values of D_A and V_A (4000 cm^{2}s^{-1}, 400 cm s^{-1}) are typical TFR values. In fact, many simulations for other impurities in medium $(5\times10^{13}$ cm$^{-3})$ to high $(1.5\times10^{14}$ cm$^{-3})$ density discharges[10,11] have shown that these values represent the center of gravity of a two-parameter distribution. The dependence of D_A and V_A on plasma properties (electron density, mass of working gas) is not yet clearly demonstrated. In part this is certainly due to the fact that the code results suffer from relatively large errors for both D_A and V_A [(25—50)% and (50—100)%, respectively], as long as only vuv spectroscopy data (no lines from the heliumlike ions) are available.

Figure 4 shows the radial abundance profiles for the H-, He-, Li-, and Be-like argon ions as given by the code. As already stated, they correspond to $t=290$ ms, but will be taken as valid for the whole interval from $t=240$ to $t=340$ ms.

Another x-ray spectrum to be presented and discussed in the following sections has been taken very early in the discharge when the electron density was much lower. In
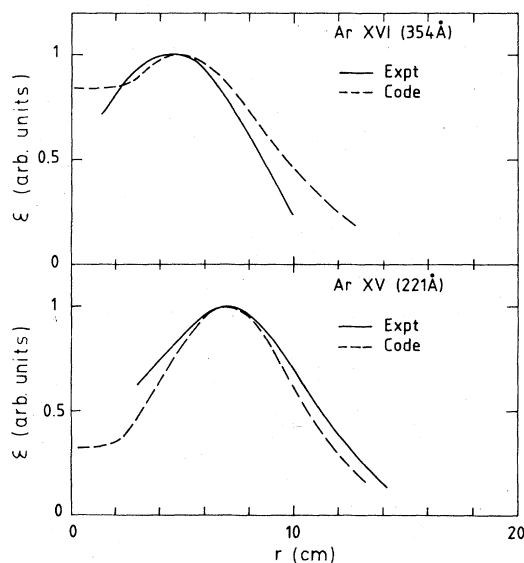

FIG. 3. Radial emissivity profiles of vuv lines of argon as observed (solid lines) during the time interval A and calculated by the impurity transport code [$n_e(0)=5.7\times10^{13}$ cm^{-3}, $D_A=4000$ cm^{2}s^{-1}, $V_A=400$ cm s^{-1}].

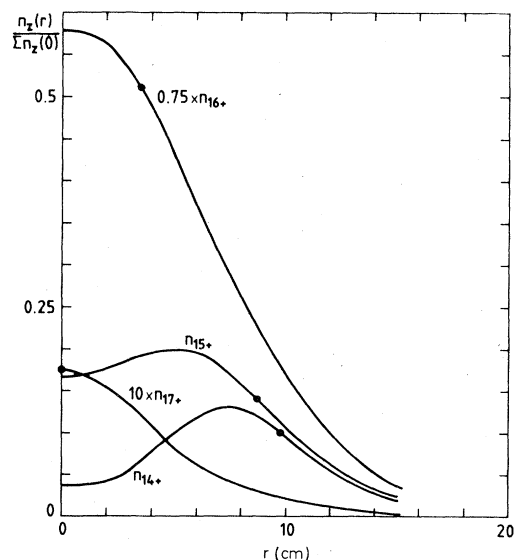FIG. 4. Radial charge-state distributions of argon ions (H-like to Be-like) as calculated by the impurity transport code for the time interval A [$n_e(0)=5.7\times10^{13}$ cm^{-3}, $D_A=4000$ cm^{2}s^{-1}, $V_A=400$ cm s^{-1}]. The densities are normalized to the total argon density at $r=0$. The points on the curves indicate the radial location of the maximum at ionization equilibrium.
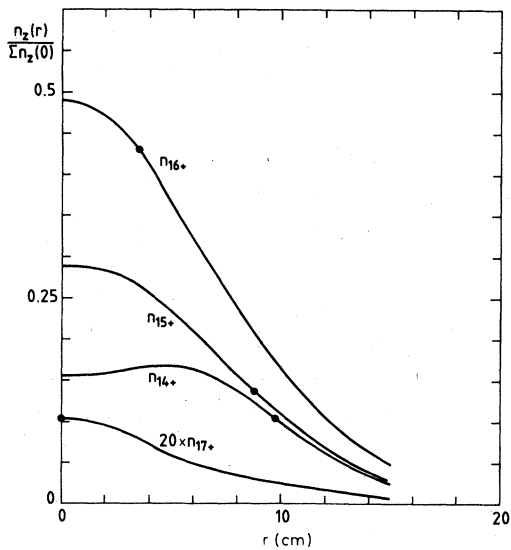
FIG. 5. Same as Fig. 4, but for case B [$n_e(0) = 2.1 \times 10^{13}$ cm^{-3}, $D_A = 5000$ cm^2 s^{-1}, $V_A = 500$ cm s^{-1}].

this case, B, the x-ray spectrum has been integrated from $t = 40$ to $t = 140$ ms. The corresponding electron-temperature profile is identical to that given in Fig. 2 (within the error bars of the Thomson scattering data). For the code calculations we have taken the electron-density-profile given by the HCN interferometer for $t = 90$ ms, i.e., again at half-time of the interval. This profile is very similar to that given in Fig. 2, but has the central value $n_e(0) = 2.1 \times 10^{13}$ cm^{-3}. As already stated, the vuv line radiances are very low in this early phase of the discharge, and it is not possible to use emissivity profiles for the adjustment of the transport parameters. We have therefore run the code with various pairs (D_A, V_A). In anticipation of what will be used in Sec. VI we show in Fig. 5 the abundance profiles calculated with $D_A = 5000$ cm^2 s^{-1} and $V_A = 500$ cm s^{-1}, without justifying this particular choice for the moment.

IV. EXPERIMENTAL X-RAY SPECTRA

The spectra have been taken with a bent-crystal spectrometer.[13] The diffracting crystal is a (20$\bar{2}$0) quartz plate, bent to a radius of 288 cm. The crystal dimensions are $5 \times 3 \times 0.04$ cm^3. The detector is a proportional counter with delay-line position encoding, working with an 80 vol% Xe—20 vol% CO_2 mixture at 1 atm. Extremely thin windows are used for the He-filled spectrometer (7-μm-thick Mylar) and for the tokamak and detector windows (both 25-μm-thick Be). A particular component of the data acquisition system is the discrimination against hard-x-ray, γ-ray, and neutron-induced events[14] which completely eliminated background from the argon spectra. The spectral resolution of the instrument is $\lambda/(d\lambda) \approx 15\,000$.

In Fig. 6(a) we show the experimental x-ray spectrum
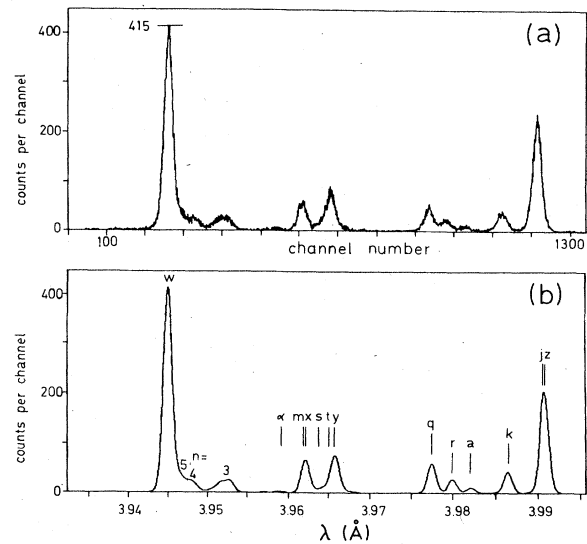
FIG. 6. X-ray spectra corresponding to case A. (a) Experimental (integrated from $t = 240$ to $t = 340$ ms). (b) Calculated with the atomic-physics and impurity transport codes ($D_A = 4000$ cm^2 s^{-1}, $V_A = 400$ cm s^{-1}).

observed during the high electron-density phase of the discharge, where we can make full use of our vuv spectroscopy equipment (case A). The spectra were integrated from $t = 240$ to $t = 340$ ms (see also Fig. 1 for the temporal behavior of line intensities). In Fig. 7(a) we show the spectrum taken during the early low-density phase of the discharge (case B, $t = 40$ to $t = 140$ ms). Obviously, the spectra are quite different with respect to relative line intensities ($w, q, j + z$). Although this will be our concern in Sec. VI, we already show here the synthetic spectra [Figs. 6(b) and 7(b)] for easier comparison.
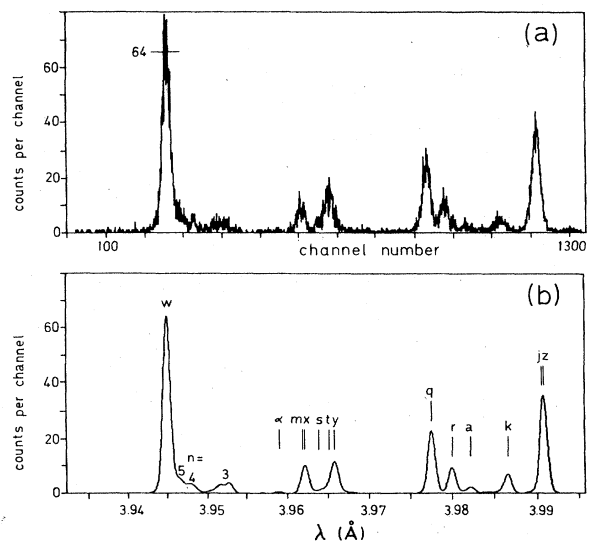

FIG. 7. X-ray spectra corresponding to case B. (a) Experimental (integrated from $t = 40$ to $t = 140$ ms). (b) Calculated ($D_A = 5000$ cm^2 s^{-1}, $V_A = 500$ cm s^{-1}).

Two final remarks must be made here. The detector used in these experiments was a single-anode wire model, which intercepts only a fraction of the photon flux from each spectral line. In order to get a good signal-to-noise ratio, the spectra were accumulated over several (typically 15) tokamak discharges (with a new multiple-anode wire detector excellent spectra will be obtained from single discharges).

The other remark is related to the value of the Bragg angle (68°) used here. Due to the high dispersion of the spectrometer, which is necessary for high spectral resolution, the x-ray spectrum of argon we are interested in (i.e., at least the spectral interval from line w to line z) is spread out over more than the physical length of the detector. In the case of Figs. 6(a) and 7(a), two subspectra at different detector settings have been taken. Both subspectra include the x,y lines, allowing for correct evaluation of relative line intensities and wavelength shifts.

V. ATOMIC-PHYSICS CALCULATIONS

The x-ray crystal spectrometer covers the spectral interval from $\lambda = 3.94$ to $\lambda = 4.01$ Å, containing the characteristic lines of the He-like ions of argon as well as dielectronic satellites from the Li- and Be-like charge states. For tokamak plasmas, radiative transfer within these lines may be neglected and the observed intensity is directly related to the emissivity, ϵ_{if}, defined by

$$\epsilon_{if} = n_i A_r^{if} , \qquad (3)$$

where A_r^{if} is the probability for the radiative transition between initial (i) and final (f) states. The density n_i of the initial state is obtained from the density n_Z of the atom ionized Z times in the ground state by a collisional-radiative model.

For the lines w, x, y, and z ($1s^2\,^1S_0$-$1s\,2p\,^1P_1$, $^3P_2$, $^3P_1$, $1s\,2s\,^3S_1$) of the heliumlike ions, we write

$$\epsilon_{if}(T_e) = n_e[n_{16}C_{if}^1(T_e) + n_{17}C_{if}^2(T_e) + n_{15}C_{if}^3(T_e)] , \qquad (4)$$

where C_{if}^1 stands for the effective rate coefficients for collisional excitation from the ground state including cascades. The radiative and dielectric recombination from the H-like ion is given by C_{if}^2. Finally, excitation by inner-shell ionization (i.e., $1s^2 2s + e \rightarrow 1s\,2s + 2e$) corresponds to C_{if}^3. For the coefficients $C_{if}^{1,2,3}$ we make use of extended calculations for the nearby element calcium.[15] In fact, Mewe *et al.*[16,17] have shown that for two elements, A and B, one has

$$C_{if}^{1,3}(A,T_e) = C_{if}^{1,3}\left[B, \left[\frac{Z_B}{Z_A}\right]^2 T_e\right]\left[\frac{Z_B}{Z_A}\right]^3 , \qquad (5)$$

where Z_A and Z_B are effective charges taking into account an electron screening effect.

Our $C_{if}^{1,3}$ data for argon have been derived from the calcium data of Ref. 15, Tables 7a and 7b, using Eq. (5) with $Z_{Ar} = 17.5$ and $Z_{Ca} = 19.5$. For the rate coefficient by recombination C_{if}^2 we use a similar Z-scaling expression:

$$C_{if}^2(A,T_e) = C_{if}^2\left[B, \left[\frac{Z_B}{Z_A}\right]^2 T_e\right]\frac{Z_A}{Z_B} . \qquad (5')$$

The calcium data are from Ref. 15, Table 7c.

The inner-shell excitation rate coefficients for the q, r, s, and t satellite lines have also been derived from the calcium data,[15] Table 7b using Eq. (5).

For the other satellite lines the main population process is dielectronic capture on the He- and Li-like ion ground states:

$$1s^2 + e \rightarrow 1s\,2pnl, \quad 1s^2 2s + e \rightarrow 1s\,2s\,2pnl , \qquad (6)$$

$$\epsilon_{if}(T_e) = n_e n_{Z+1} F_2^*(if) F_1^*(i,T_e) ,$$

$$F_2^*(if) = \frac{\omega_i}{\omega_g} A_a^{ig} A_r^{if}\left[\sum_{j'} A_a^{ij'} + \sum_{f'} A_r^{if'}\right]^{-1} , \qquad (7)$$

$$F_1^*(i,T_e) = \frac{1}{2}\left[\frac{2\pi\hbar^2}{mkT_e}\right]^{3/2}\exp\left[-\frac{E_{ig}}{kT_e}\right] , \qquad (8)$$

where n_{Z+1} is the ground-level density of the recombining ion ($Z + 1$ times ionized) and ω_g its statistical weight. ω_i is the statistical weight of the upper level of the line, A_r^{if} and A_a^{ig} are the radiative and autoionization transition probabilities from levels i to f and i to g, respectively. The sum over f' extends over all levels of the Z ion lower than i, the sum over j' extends over all levels j' of the $Z + 1$ ion which can be populated by autoionization of i. E_{ig} is the energy of the free electron after the autoionization of the level i to g.

The wavelengths λ, the radiative probabilities A_r^{if}, and the sum of all the probabilities to all lower levels $\sum_{f'} A_r^{if'}$ have been calculated with the program SUPER STRUCTURE developed by Eissner *et al.*[18] The autoionization probabilities A_a^{ig} and $\sum_{j'} A_a^{ij'}$ for all the available continua have been obtained with the program AUTOLSJ described by TFR Group *et al.*[5] These programs are appropriate for the calculation of large quantities of atomic data as they use model potentials. These are scaled Thomas-Fermi-Dirac potentials where the scaling parameters λ_s, λ_p, λ_d have been determined by a minimization of the following configurations: $1s^2 2s$, $1s\,2s\,2p$, $1s^2 3d$, $1s\,2p\,3d$ ($\lambda_s = 2.079$, $\lambda_p = 1.810$, $\lambda_d = 1.932$, $\lambda_f = 1$). The monoelectronic wave functions (orbitals) derived from these potentials have been used for the He- and Be-like ions. Table I gives the Ar XVI $n = 2$ dielectronic satellite atomic data for the observed lines: (1) Vainshtein and Safronova,[19,20] (2) Bhalla and Tunnel,[21] (3) present work. In the Vainshtein and Safronova calculations of energies and wavelengths the relativistic energy matrix is developed as an expansion in powers of $1/Z$ on a basis of nonrelativistic He-like wave functions including the continuum. However for radiative and autoionization transition probability calculations the authors restrict the configuration basis to the complex corresponding to the configuration of the level considered. In the calculations of Bhalla and Tunnell the relativistic Hamiltonian includes the relativistic corrections in the Hartree-Fock-Slater atomic model. This approximate Hamiltonian is diagonalized on Hartree-Fock configuration basis inside each complex. All the atomic parameters have been calculated with the same wave functions. In our calculations the relativistic Hamiltonian is separated in one-body and two-body terms

TABLE I. Ar XVI n=2 dielectronic satellite data. A_a, A_r, and $F_2^*(if)$ in units of 10^{13} s^{-1}. Key letters are from Ref. 1.

Array	Key	Vainshtein and Safronova (Refs. 19 and 20)				Bhalla and Tunnel (Ref. 21)				Present work			
		λ (Å)	A_a	A_r	$F_2^*(if)$	λ (Å)	A_a	A_r	$F_2^*(if)$	λ (Å)	A_a	A_r	$F_2^*(if)$
$1s2p^2\,^2D_{5/2}-1s^22p\,^2P_{3/2}$	j	3.9932	18.30	5.19	24.30	3.9898	14.35	4.88	21.86	3.9907	15.19	5.11	22.95
$1s2s2p\,^2P_{3/2}-1s^22s\,^2S_{1/2}$	q	3.9806	0.134	10.1	0.53	3.9785	0.24	9.56	0.96	3.9777	0.26	10.08	1.03
$1s2s2p\,^2P_{1/2}-1s^22s\,^2S_{1/2}$	r	3.9827	1.26	8.70	2.20	3.9807	1.29	8.23	2.24	3.9801	1.56	8.52	2.64
$1s2p^2\,^2D_{3/2}-1s^22p\,^2P_{1/2}$	k	3.9892	17.30	6.04	17.30	3.9865	13.46	2.29	6.41	3.9866	14.44	5.84	16.64
$1s2p^2\,^2P_{3/2}-1s^22p\,^2P_{3/2}$	a	3.9852	1.33	14.0	4.88	3.9826	1.14	9.86	2.92	3.9823	0.97	13.73	3.37
$1s2s2p\,^2P_{3/2}-1s^22s\,^2S_{1/2}$	s	3.9669	12.0	0.43	1.65	3.9639	9.69	0.51	1.84	3.9640	10.28	0.55	2.07
$1s2s2p\,^2P_{1/2}-1s^22s\,^2S_{1/2}$	t	3.9677	10.8	1.86	3.18	3.9651	8.59	1.83	3.01	3.9652	9.03	2.13	3.44
$1s2p^2\,^2S_{1/2}-1s^22p\,^2P_{3/2}$	m	3.9651	2.85	4.00	3.33	3.9616	2.08	3.87	2.37	3.9620	2.26	4.08	2.57

similar to the development of Vainshtein and Safronova. Here again, all the atomic data are calculated with the same wave functions obtained by diagonalization of a large basis set including all the n=2,3,4,5 configurations. It should be noted that the three sets of theoretical values for A_r, A_a, and $F_2^*(if)$ are in good agreement (except for the k line). However for the wavelengths there is a systematic difference between the first authors and the others. This could be explained by the inclusion of the continuum in the energy expansion. In Table II are given the atomic data for the n=3 and n=4 satellite lines with $F_2^*(if) \geq 5.0 \times 10^{12}$ s^{-1} corresponding to Ref. 21 and present calculations (Ref. 20 does not contain n=4 data).

An extended data set for the n=5 satellite lines (not shown here) has been used to extrapolate the $n \geq 6$ satellite data. To do this, the n=5 satellite lines have been separated into four groups: odd or even upper level, convergence on w or y. Each one of these four groups is spread over a narrow wavelength interval and is therefore represented by a single, equivalent line defined by

$$\lambda(n) = \frac{\sum_i \lambda_i F_2^*(if)}{\sum_i F_2^*(if)},$$

$$F_2^*(n) = \sum_i F_2^*(if).$$

For the extrapolation to higher n we use the relations $F_2^*(n)n^3 = \text{const}$, and $[\lambda_w - \lambda(n)]n^3 = \text{const}$. The results are given in Table III. Finally, the atomic data for the n=2,3,4 satellite lines produced by dielectronic recombination from the Li-like charge state $[Z + 1 = 15$ in Eq. (6)] to the Be-like charge state are given in Table IV.

VI. COMPARISON OF EXPERIMENTAL AND SYNTHETIC SPECTRA

The experimental x-ray spectra are line-of-sight integrated emissivities. Consequently, the synthetic spectra are obtained by integration of Eqs. (4) and (6), taking the local values of T_e from Thomson scattering, n_e from interferometry, and charge-state distributions from the impurity transport code (Sec. III). The complete atomic-physics data package of Sec. V is used. We also introduce a Doppler temperature common to all species (see below). Finally, the intensity of the w line is normalized to its experimental value.

We start with the spectrum of the highest signal-to-noise ratio, i.e., case A, taken during the high-electron-density phase of the discharge. The observed and synthetic spectra are given in Figs. 6(a) and 6(b), respectively. The overall agreement between the observed and computed spectra is quite good. In particular this is true for the $n > 2$ satellite contributions to the long-wavelength wing of the w line and for the asymmetry of the y line, mainly due to the weak satellites s and t.

In Table V are given the wavelength shifts of the most prominent lines with respect to the resonance line w (3.9451 Å, present work). It should be noted that the experimental data have been read from a high-resolution

TABLE II. Ar XVI $n=3$ and 4 dielectronic satellite data. A_a, A_r, and $F_2^*(if)$ in units of 10^{13} s^{-1}.

Array	λ (Å)	A_a	A_r	$F_2^*(if)$	λ (Å)	A_a	A_r	$F_2^*(if)$
		Bhalla and Tunnel (Ref. 21)				Present work		
$1s\,2p\,3s\ ^2P_{1/2}-1s^2 3s\ ^2S_{1/2}$	3.9633	3.56	1.62	2.15	3.9628	3.70	1.52	2.14
$1s\,2p\,3p\ ^2P_{3/2}-1s^2 3s\ ^2S_{1/2}$	3.9596	3.87	0.62	2.08	3.9590	4.07	0.55	1.93
$1s\,2p\,3s\ ^2P_{1/2}-1s^2 3s\ ^2S_{1/2}$	3.9514	1.27	8.13	2.13	3.9504	1.12	8.42	1.93
$1s\,2p\,3s\ ^2P_{3/2}-1s^2 3s\ ^2S_{1/2}$	3.9520	0.79	8.15	2.77	3.9509	0.64	8.53	2.31
$1s\,2p\,3d\ ^2F_{7/2}-1s^2 3d\ ^2D_{5/2}$	3.9491	1.33	8.56	8.63	3.9479	1.37	8.74	9.45
$1s\,2p\,3d\ ^2F_{5/2}-1s^2 3d\ ^2D_{3/2}$	3.9478	1.28	6.66	4.95	3.9466	1.31	6.66	5.33
$1s\,2p\,3s\ ^2F_{5/2}-1s^2 3d\ ^2D_{5/2}$	3.9481	1.28	1.68	1.25	3.9470	1.31	1.87	1.50
$1s\,2p\,3p\ ^2D_{5/2}-1s^2 3p\ ^2P_{3/2}$	3.9640	2.65	0.63	1.73	3.9643	2.67	0.60	1.66
$1s\,2p\,3p\ ^2D_{3/2}-1s^2 3p\ ^2P_{1/2}$	3.9515	3.32	8.35	8.88	3.9518	3.45	8.58	9.51
$1s\,2p\,3p\ ^2D_{5/2}-1s^2 3p\ ^2P_{3/2}$	3.9523	4.06	8.40	15.97	3.9529	3.67	8.70	15.05
$1s\,2p\,3p\ ^2P_{3/2}-1s^2 3p\ ^2P_{3/2}$	3.9513	1.46	9.08	4.50	3.9516	0.95	9.50	3.16
$1s\,2p\,3p\ ^2S_{1/2}-1s^2 3p\ ^2P_{3/2}$	3.9447	1.15	5.83	1.56	3.9457	0.97	6.19	1.38
$1s\,2s\,4p\ ^2P_{1/2}-1s^2 4s\ ^2S_{1/2}$	3.9649	1.77	0.29	0.42	3.9646	1.57	0.43	0.58
$1s\,2p\,4d\ ^2D_{5/2}-1s^2 4d\ ^2D_{3/2}$	3.9479	0.07	7.02	0.29	3.9470	0.07	3.42	0.14
$1s\,2p\,4d\ ^2F_{5/2}-1s^2 4d\ ^3D_{3/2}$	3.9473	0.64	6.83	2.38	3.9465	0.64	6.87	2.43
$1s\,2p\,4d\ ^2F_{5/2}-1s^2 4d\ ^2D_{5/2}$	3.9474	0.84	3.36	1.17	3.9466	0.64	3.34	1.18
$1s\,2s\,4s\ ^2S_{1/2}-1s^2 4p\ ^2P_{1/2}$	3.9745	0.86	0.15	0.20	3.9742	0.83	0.25	0.27
$1s\,2s\,4s\ ^2S_{1/2}-1s^2 4p\ ^2P_{3/2}$	3.9750	0.86	0.24	0.32	3.9749	0.83	0.44	0.47
$1s\,2p\,4p\ ^4D_{5/2}-1s^2 4p\ ^2P_{3/2}$	3.9714	0.08	0.11	0.20	3.9702	0.10	0.13	0.32
$1s\,2p\,4p\ ^2D_{3/2}-1s^2 4p\ ^2P_{1/2}$	3.9496	1.06	10.16	3.70	3.9483	1.16	10.07	4.10
$1s\,2p\,4p\ ^2D_{5/2}-1s^2 4p\ ^2P_{3/2}$	3.9499	0.89	10.38	4.80	3.9487	0.99	10.31	5.26

display of the original spectrum taking all channels, whereas the display used for Figs. 6(a) and 7(a) shows only every third channel. For the experimental $\Delta\lambda$ we estimate the error to be approximately 0.1 mÅ, i.e., $\sim\frac{1}{10}$ of the Doppler width. However, for the line α [for which the intensity scale of Fig. 6(a) is not adequate but which is evident in the original data] we add another 0.1 mÅ for reasons of photon statistics. Finally, as the experimental spectrum is the composite of two subspectra (see Sec. III), we add an estimated fitting error of 0.1 mÅ for the lines concerned. As seen from Table V, the observed line positions agree quite well with the calculations. However, the

TABLE III. Ar XVI $n \geq 5$ dielectronic satellite data. $F_2^*(n)$ in units of 10^{13} s^{-1}. In the upper-level column, o (e) denotes odd (even).

n	Upper level	Convergence on w $\lambda(n)$	$F_2^*(n)$	Convergence on y $\lambda(n)$	$F_2^*(n)$
5	o	3.9460	5.04	3.9664	1.04
	e	3.9467	5.93	3.9679	1.27
6	o	3.9456	2.92	3.9662	0.60
	e	3.9460	3.43	3.9671	0.73
7	o	3.9454	1.84	3.9661	0.38
	e	3.9457	2.16	3.9666	0.46
8	o	3.9453	1.23	3.9660	0.25
	e	3.9455	1.45	3.9664	0.31
9	o	3.9453	0.86	3.9660	0.18
	e	3.9454	1.02	3.9662	0.22
10	o	3.9452	0.63	3.9660	0.13
	e	3.9453	0.74	3.9662	0.16

difference between calculated and observed wavelength shifts (typically $+0.6$ mÅ) is outside the experimental error.

Turning now to relative line intensities, we first remember that the $(j+z)/w$ ratio is only weakly dependent on the charge-state distributions, as all three lines have He-like parents (z has weak contributions from recombination and inner-shell ionization). The computed ratio, however, critically depends on the rates for collisional excitation and dielectronic recombination. The degree of agreement between the observed (0.56) and computed (0.5) values for this line ratio corresponds to the state of the art in atomic-physics calculations and T_e measurements.

Another interesting line ratio is q/w. In contrast to $(j+z)/w$, this ratio depends on T_e through the local densities of the Li-like and He-like ions. In view of this direct dependence the agreement between observed (0.13 ± 0.01) and calculated (0.14) values for the q/w ratio is surprisingly good.

As already said, the synthetic spectrum is the result of two codes in cascade: an atomic-physics code and an impurity transport code, which in turn relies on vuv spectroscopy observations. Consequently, the good agreement between observed and computed spectra does not, "per se," verify both codes independently. However, it is reasonably fair to conclude that, given the actual state of plasma spectroscopy (photon statistics, summing over several shots, etc.), the codes are quite adequate.

We turn now to the spectrum of Fig. 7(a), taken during the low-density phase of the discharge (case B). As already said, the electron temperature is constant during these particular discharges, reaching the value of 1.25 keV

TABLE IV. Ar XV $n=2,3,4$ dielectronic satellite data. A_a, A_r, and F_2^* (if) in units of 10^{13} s^{-1}.

Array	λ (Å)	A_a	$\sum A_a$	A_r	$F_2^*(if)$
$1s\,2s\,2p^2\,{}^3D_1 - 1s^2 2s\,2p\,{}^3P_0$	4.0162	10.51	12.53	7.52	5.62
$1s\,2s\,2p^2\,{}^3D_1 - 1s^2 2s\,2p\,{}^3P_2$	4.0215	10.51	12.53	1.06	0.80
$1s\,2s\,2p^2\,{}^3D_2 - 1s^2 2s\,2p\,{}^3P_1$	4.0176	13.49	15.49	6.55	9.96
$1s\,2s\,2p^2\,{}^3D_3 - 1s^2 2s\,2p\,{}^3P_2$	4.0205	15.30	17.47	5.17	12.23
$1s\,2s\,2p^2\,{}^3P_1 - 1s^2 2s\,2p\,{}^3P_1$	4.0156	4.86	7.49	6.58	2.45
$1s\,2s\,2p^2\,{}^3P_1 - 1s^2 2s\,2p\,{}^3P_1$	4.0193	4.86	7.49	4.58	1.70
$1s\,2s\,2p^2\,{}^3P_2 - 1s^2 2s\,2p\,{}^3P_2$	4.0166	1.91	4.43	12.90	3.29
$1s\,2s\,2p^2\,{}^3S_1 - 1s^2 2s\,2p\,{}^3P_1$	3.9997	5.55	9.50	1.51	0.86
$1s\,2s\,2p^2\,{}^3S_1 - 1s^2 2s\,2p\,{}^3P_2$	4.0023	5.55	9.50	3.08	1.76
$1s\,2s\,2p^2\,{}^1D_2 - 1s^2 2s\,2p\,{}^1P_1$	4.0300	11.32	26.89	3.88	3.52
$1s\,2s\,2p^2\,{}^3P_2 - 1s^2 2s\,2p\,{}^1P_1$	4.0262	4.33	21.66	1.43	0.66
$1s\,2s\,2p^2\,{}^1S_0 - 1s^2 2s\,2p\,{}^1P_1$	4.0095	6.58	21.95	5.53	0.66
$1s\,2s\,2p\,3d\,{}^3F_2 - 1s^2 2s\,3d\,{}^3D_1$	3.9853	0.69	3.72	3.48	0.60
$1s\,2s\,2p\,3d\,{}^3F_3 - 1s^2 2s\,3d\,{}^3D_2$	3.9841	0.71	2.77	2.75	0.71
$1s\,2s\,2p\,3d\,{}^3F_3 - 1s^2 2s\,3d\,{}^3D_3$	3.9844	0.71	2.77	3.97	1.00
$1s\,2s\,2p\,3d\,{}^3F_4 - 1s^2 2s\,3d\,{}^3D_3$	3.9826	1.12	2.34	8.10	3.89
$1s\,2s\,2p\,3d\,{}^1F_3 - 1s^2 2s\,3d\,{}^1D_2$	3.9841	0.62	3.90	6.13	1.20
$1s\,2s\,2p\,3p\,{}^3D_2 - 1s^2 2s\,3p\,{}^3D_1$	3.9914	1.06	4.19	4.13	0.88
$1s\,2s\,2p\,3p\,{}^3D_3 - 1s^2 2s\,3p\,{}^3P_2$	3.9898	1.12	2.92	6.97	2.50
$1s\,2p^2 3s\,{}^5P_3 - 1s^2 2s\,3p\,{}^3P_2$	3.9892	0.37	0.80	1.60	0.79
$1s\,2s\,2p\,3p\,{}^1D_2 - 1s^2 2s\,3p\,{}^1P_1$	3.9857	2.50	4.80	8.56	3.54
$1s\,2s\,2p\,3p\,{}^3D_3 - 1s^2 2s\,3p\,{}^3P_2$	3.8779	1.93	1.27	1.33	6.00
$1s\,2s\,2p\,4d\,{}^3F_3 - 1s^2 2s\,4d\,{}^3D_2$	3.9819	0.42	2.05	3.73	0.53
$1s\,2s\,2p\,4d\,{}^3F_3 - 1s^2 2s\,4d\,{}^3D_3$	3.9820	0.42	2.05	4.23	0.60
$1s\,2s\,2p\,4d\,{}^3F_4 - 1s^2 2s\,4d\,{}^3D_3$	3.9802	0.60	1.25	9.50	2.37
$1s\,2s\,2p\,4d\,{}^1F_3 - 1s^2 2s\,4d\,{}^1D_2$	3.9795	0.73	0.89	9.54	2.20
$1s\,2s\,2p\,4p\,{}^3D_2 - 1s^2 2s\,4p\,{}^3P_2$	3.9840	0.63	2.72	4.03	0.56
$1s\,2s\,2p\,4p\,{}^3D_3 - 1s^2 2s\,4p\,{}^3P_2$	3.9820	0.67	1.46	9.55	1.95
$1s\,2s\,2p\,4p\,{}^3P_2 - 1s^2 2s\,4p\,{}^3P_1$	3.9812	0.59	1.36	5.45	0.96
$1s\,2s\,2p\,4p\,{}^1D_2 - 1s^2 2s\,4p\,{}^3P_2$	3.9810	0.96	1.88	3.18	0.63
$1s\,2s\,2p\,4p\,{}^1D_2 - 1s^2 2s\,4p\,{}^1P_1$	3.9814	0.96	1.88	6.75	1.34

very early in the discharge. Consequently, we expect only minor changes for those line-intensity ratios which depend on T_e mainly through the excitation rates rather than through the ratio of charge-state abundances. Indeed, for the $(j+z)/w$ intensity ratio we observe 0.58. A striking difference, however, exists for the q/w ratio, which is 0.37, i.e., three times higher than during the high-density phase of the discharge. Consequently, the charge-state distribution in the hot plasma core must be displaced to lower ion charges, i.e., still further away from

TABLE V. Wavelength shifts with respect to the resonance line w. α denotes $1s\,2p\,3s\,{}^2P_{3/2} - 1s^2 3s\,{}^2S_{1/2}$ and $\lambda_w = 3.9451$ Å.

Key	$\Delta\lambda_{\text{expt}}$ (mÅ)	$\Delta\lambda_{\text{theor}}$ (mÅ)
α	13.6±0.2	13.9
x	16.6±0.1	17.1
y	20.2±0.1	20.8
q	32.2±0.1	32.6
r	34.2±0.2	35.0
a	36.4±0.2	37.2
k	40.9±0.2	41.5
j	45.0±0.2	45.6
z		45.8

ionization equilibrium than in case A. To get a quantitative hold of this observation we make use of synthetic spectra. However, the impurity transport code cannot be used here in the same way as for case A, the intensities of the vuv spectrum lines being far too low to allow the determination of the transport coefficients D_A and V_A. We therefore adopt the following procedure. The impurity transport code is run with various values for D_A and V_A, the only experimental input data being the T_e and n_e profiles. The calculated charge-state distributions are then fed into the second code which calculates the corresponding x-ray spectra. The comparison of computed and observed q/w intensity ratios then permits the determination of V_A and D_A.

Good agreement is obtained for $D_A = 5000$ cm^2 s^{-1} and $V_A = 500$ cm s^{-1}. Figure 5 shows the corresponding ion abundance profiles. The synthetic x-ray spectrum is shown in Fig. 7(b). The calculated value $q/w = 0.35$ agrees with the experiment (0.36) given the error from photon statistics. It is interesting to note that with $D_A = 4000$ cm^2 s^{-1} and $V_A = 400$ cm s^{-1}, i.e., the values corresponding to the high-density case A, the calculated q/w intensity ratio is too low by 20%, which is certainly outside the experimental error. In other words, again we

observe a deviation from ionization equilibrium, the deviation being higher at lower electron density. However, the density effect taken alone does not correctly reproduce the observed spectrum. The diffusion coefficient D_A must be increased from 4000 to 5000 cm^2 s^{-1} (changes in V_A having a less-pronounced effect, we have kept constant the convection parameter S).

Small variations of the D_A and V_A values induce changes in the emissivities of the vuv lines which, in general, are inside the experimental uncertainties. With the extension to x-ray line spectroscopy as proposed here, the determination of the transport coefficients becomes more accurate. This is due to the fact that line emission from the plasma center is introduced into the code. From the instrumental point of view the advantage of x-ray crystal spectroscopy is that line radiation from the various ionization stages[5] is observed within a narrow wavelength band, thus avoiding the problem of spectral calibration.

VII. ION-TEMPERATURE MEASUREMENTS

The width of the spectral lines observed with the crystal spectrometer is dominated by Doppler broadening with only a small contribution from the natural linewidth and from instrumental broadening. In general, the best candidate for the determination of the ion temperature T_i is the intense line w. However, the close, $n > 3$ dielectronic satellites on the long-wavelength wing of this line contribute to its apparent Doppler width. This difficulty may be overcome by a multiple-Voigt-function best fit or, less rigorously, by an adequate choice of the fitting channels in a single-Voigt-function approach.

In the case of argon we have found it advantageous to use the $j + z$ feature. From Sec. V we know that these lines are separated by 0.2 mÅ. Treating them as a single line leads to an overestimation of T_i which, in the worst case of equal intensities, amounts to approximately 10% at $T_i = 0.5$ keV. On the other hand there are no close satellite lines with He-like-ion parents which could contribute to the profile. In practice, this advantage over the line w is demonstrated by the fact that the value for T_i which we find from a single-line fit does not depend on
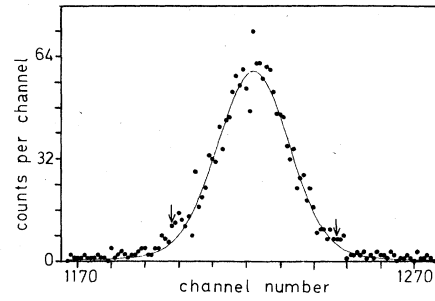

FIG. 8. Single-Voigt-function fit to the $j + z$ line of Fig. 7(a). The ion Doppler temperature is $T_i = 458 \pm 28$ eV. The arrows indicate the range used for the fit. The channel width is 0.0447 mÅ.

the range used for the fit. In Fig. 8 we show the result of a Doppler fit for the $j + z$ line from case A [Fig. 7(a)].

VIII. CONCLUSION

Ab initio calculations for the wavelengths and atomic parameters have been carried out for the dielectronic and inner-shell satellite lines of the Ar^{16+} resonance line. These data, together with spatial ion charge-state distributions obtained by an impurity transport code were used to calculate x-ray spectra. These synthetic spectra were compared to experimental ones, obtained from TFR tokamak discharges with a high-resolution crystal spectrometer. The good agreement between synthetic and experimental spectra at high-electron density demonstrates the quality of the impurity transport and atomic-physics codes. A low-electron-density case has shown that fitting of calculated-line intensity ratios to observed values may lead to a better description of anomalous transport throughout the various phases of the discharge (high-throughput, high-contrast crystal spectrometers now available on TFR and other tokamaks allow increased time resolution and single-discharge exposure). Finally it should be noted that the analysis of our x-ray spectra of argon may be applied easily to other tokamak plasma impurities, in particular to those also of interest in solar-flare physics.

*M. H. Achard, J. Adam, J. Andreoletti, P. Bannelier, H. Barkley, J. F. Bonnal, C. Breton, J. Breton, R. Brugnetti, J. L. Bruneau, M. Calderon, R. Cano, H. Capes, M. Charet, M. Chatelier, A. Cohen, M. Cotsaftis, J. P. Crenn, B. De Gentile, C. De Michelis, H. W. Drawin, J. Druaux, M. Dubois, J. L. Duranceau, A. Fissolo, M. Fois, D. Gambier, A. Geraud, F. Gervais, P. Giovannoni, A. Grosman, W. Hecq, T. Hutter, L. Jacquet, J. Johner, H. Kuus, J. Lasalle, L. Laurent, O. Lazare, P. Lecoustey, F. Linet, G. Martin, E. Maschke, M. Mattioli, R. Oberson, J. Olivain, M. Pain, P. Platz, A. L. Pecquet, L. Pignol, A. Quemeneur, J. Ramette, L. Rebuffi, C. Reverdin, J. P. Roubin, A. Samain, B. Saoutic, F. Simonet, R. Soubaras, J. Tachon, J. Touche, B. Tournesac, D. Veron, B. Zanfagna.

[1] A. H. Gabriel, Mon. Not. R. Astron. Soc. **160**, 99 (1972).

[2] J. Dubau and S. Volonte, Rep. Prog. Phys. **43**, 199 (1980).

[3] S. Von Goeler, M. Bitter, S. Cohen, D. Eames, K. W. Hill, D. Hills, R. Hulse, G. Lenner, D. Manos, P. Roney, W. Roney, N. Sauthoff, S. Sesnic, W. Stodiek, F. Tenney, and J. Timberlake, in *Proceedings of the Course on Diagnostics for Fusion Reactor Conditions, Varenna, Italy, 1982*, edited by P. E. Stott *et al.* (Commission of the European Communities, Brussels, 1983), Vol. I, p. 109.

[4] M. Bitter, K. W. Hill, N. R. Sauthoff, P. C. Efthimion, E. Meservey, W. Roney, S. Von Goeler, R. Horton, M. Goldman, and W. Stodiek, Phys. Rev. Lett. **43**, 129 (1979).

[5] TFR Group, J. Dubau, and M. Loulergue, J. Phys. B **15**, 1007 (1981).

[6]F. Bely-Dubau, P. Faucher, L. Steenman-Clark, M. Bitter, S. Von Goeler, K. W. Hill, C. Camhy-Val, and J. Dubau, Phys. Rev. A **26**, 3459 (1982).

[7]TFR Group and F. Bombarda, in *Proceedings of the 11th European Conference on Controlled Fusion and Plasma Physics, Aachen, FRG, 1983*, edited by S. Methfessel (European Physical Society, Aachen, 1983).

[8]E. Källne, J. Källne, A. Dalgarno, E. S. Marmar, J. E. Rice, and A. K. Pradhan, Phys. Rev. Lett. **52**, 2245 (1984).

[9]TFR Group, Nucl. Fusion **23**, 559 (1983).

[10]C. Breton, C. De Michelis, M. Finkenthal, and M. Mattioli, J. Phys. E **12**, 894 (1979).

[11]C. Breton, A. Compant La Fontaine, C. De Michelis, W. Hecq, J. Lasalle, P. Lecoustey, M. Mattioli, G. Mazzitelli, P. Platz, and J. Ramette, J. Phys. B **16**, 2627 (1983).

[12]A. Burgess and M. C. Chidichimo, Mon. Not. R. Astron. Soc. **203**, 1269 (1983).

[13]P. Platz, J. Ramette, E. Belin, C. Bonnelle, and A. Gabriel, J.

Phys. E **14**, 448 (1981).

[14]F. Bombarda, J. P. Coulon, P. Platz, and J. Ramette, Nucl. Instrum. Methods **222**, 563 (1984).

[15]F. Bely-Dubau, J. Dubau, P. Faucher, A. H. Gabriel, M. Loulergue, L. Steenman-Clark, S. Volonte, E. Antonucci, and C. G. Rapley, Mon. Not. R. Astron. Soc. **201**, 1155 (1982).

[16]R. Mewe, J. Schrijver, and J. Sylvester, Astron. Astrophys. **87**, 55 (1980).

[17]R. Mewe, J. Schrijver, and J. Sylvester, Astron. Astrophys. Suppl. Ser. **40**, 323 (1980).

[18]W. Eissner, M. Jones, and H. Nussbaumer, Comput. Phys. Commun. **8**, 270 (1974).

[19]L. A. Vainshtein and U. I. Safronova, At. Data Nucl. Data Tables **21**, 49 (1978).

[20]L. A. Vainshtein and U. I. Safronova, At. Data Nucl. Data Tables **25**, 311 (1980).

[21]C. P. Bhalla and T. W. Tunnel, J. Quant. Spectrosc. Radiat. Transfer **32**, 141 (1984).